Directionality of FIV3 Ground Motion Intensities during the February 6, 2023 Kahramanmaraş, Türkiye Earthquake Doublet

Miguel Bravo-Haro, [a)] M. EERI, Pablo Heresi, [b)] M. EERI , Héctor Dávalos [c)], and Eduardo Miranda, [d)] M. EERI

[a] *Department of Engineering; City, University of London, Northampton Square, London EC1V 0HB, UK.*

[b] *Department of Civil Engineering, University of Chile, Av. Blanco Encalada 2002, Santiago, Chile.*

[c] *Universidad Panamericana, Facultad de Ingeniería, Álvaro del Portillo 49, Zapopan, Jalisco, 45010, México.*

[d] *John A. Blume Earthquake Engineering Center, Department of Civil and Environmental Engineering, Stanford University, Stanford, CA 94305, U.S.A.*

Abstract

At present time, ground motion prediction models neglect the directionality observed in horizontal components of earthquake ground motions, that is, the important changes in ground motion intensity that occur with changes in azimuth. This study presents an investigation of the directionality of a recently proposed measure of ground motion intensity during the February 6, 2023, M_w 7.8 Pazarcık and M_w 7.5 Elbistan earthquake doublet in the Kahramanmaraş region of Türkiye, which resulted in the collapse of more than 35,000 buildings and caused almost 60,000 fatalities. The studied intensity measure is referred to as FIV3, which has been shown to be better correlated with structural collapse than the spectral acceleration at the fundamental period of the structure. The improved intensity measure is period-dependent and is computed as the sum of the three largest incremental velocities with the same polarity obtained from the area under segments of a low-pass filtered ground acceleration time series. The following aspects are studied in this article: variation of FIV3 intensity with changes in the orientation; variation of FIV3 intensity with changes in the period of vibration; attenuation of FIV3 intensities with increasing distance; and spatial distribution of the orientation of maximum FIV3 intensity. This study is based on 231 pairs of records from the M_w 7.8 main event and 222 pairs of records from the M_w 7.5 event. Similarly to the directionality of spectral ordinates, it is found that the directionality of FIV3 intensity also increases with increasing period. Strong directionality occurred not only in the near field but up to distances as large as 400 km from the epicenter. The orientation of maximum FIV3 intensity is found to occur close to the transverse orientation, consistent with observations for the orientation of maximum spectral ordinates during strike-slip earthquakes.

1. INTRODUCTION

On February 6, 2023, two large destructive strike-slip earthquakes affected the Kahramanmaraş region of south-central Türkiye and north-western Syria. The Pazarcık earthquake was the mainshock and had a moment magnitude (M_w) of 7.8, epicenter located approximately 15 km east of the East Anatolian Fault (EAF), a focus at a depth of 8.6 km, and occurred at 4:17am local time (01:17 UTC). Approximately 9 hours later, at 15:17 local time (10:24 UTC), the M_w 7.5 Elbistan earthquake started 90 km north of the EAF, with a depth of 7.0 km. These events occurred in two different faults of a complex strike-slip faulting system controlled by the multi-junction between the Anatolian, Arabian, and African plates. Considering the high seismic hazard of this region (Gülerce et al., 2017) these two large events were not surprising. However, the magnitudes of both events were larger than that of any recorded earthquake in the area (Ambraseys, 1989) and therefore larger than any characteristic earthquake magnitude considered in state-of-the-art probabilistic seismic hazard analyses of the region (Gülerce et al., 2017). Among the historic earthquakes in the region, there are at least 5 events with estimated magnitudes ranging from 7.0 to 7.5 that occurred between 1513 and 1893. Importantly, these pre-instrumental historical records show that these earthquakes were associated to the rupture of individual segments of the EAF, unlike this "superevent" that unzipped multiple segments at once (Dal Zilio & Ampuero, 2023), resulting in a longer rupture length and larger magnitude. The combined Turkish and Syrian official fatalities from this doublet amounts to almost fifty thousand (Ozkula et al., 2023), placing it among the deadliest of the 21st century. Even more, according to initial estimates, the direct infrastructure loss exceeds $34 billion (Ozkula et al., 2023), becoming one of the costliest earthquake sequences on record.

Corresponding author: Héctor Dávalos, Email: hdavalos@up.edu.mx, Universidad Panamericana. Facultad de Ingeniería. Álvaro del Portillo 49, Zapopan, Jalisco, 45010, México.

The two main events of the 2023 Kahramanmaraş earthquake sequence were mainly bilateral strike-slip ruptures, according to a first-order analysis of the rupture process based on both satellite and seismic data (Goldberg et al., 2023; Mai et al., 2023). The M_w 7.8 mainshock began approximately 30 km south from the EAF main branch, on a north-east-striking fault consistent with the previously mapped Sakçagöz and Narlı segment of the Dead Sea Fault (DSF) (Emre et al., 2018). The rupture rapidly propagated north to the Pazarcık segment of the EAF (~10 s) and continued rupturing northeast (~125 km) and southwest (~140 km) along the Erkenek and Amanos segments of the EAF, respectively. Recent evidence has shown that, in the southwest flank of the latter segment, the speed of the back-propagating rupture signal exceeded the local shear-wave velocity, suggesting discrete episodes of super-shear rupture (Okuwaki et al., 2023). Although the rupture ended abruptly in the northeast segment after approximately 55 s, the movement continued towards the southeast for roughly 30 s more. Such rupture kinematics reveals 3 main areas of fault slip, reaching up to 7 m of slip close to the surface near the merging point of the Sakçagöz and Narlı segment and the main branch of the EAF, as well as 4 to 7 m in the southernmost segment of EAF. In the latter, corresponding to the fault extremity in the Hatay-Antakya region, there is a section with high slip (i.e., ~7 m) right before the rupture suddenly stops, resulting in stopping phases (Mai et al., 2023; Savage, 1965). Such feature, coupled with rupture directivity along the ~140 km in the southwest branch and local site effects, might explain the intense ground motions and subsequent widespread damage in the Hatay-Antakia region.

The M_w 7.5 subsequent event commenced around 90 km north of the M_w 7.8 epicenter on the Sürgü-Çardak Fault (Taymaz et al., 1991). This is a left-lateral fault that meets the EAF to the east, and ruptured bilaterally over ~150 to 170 km and to a depth of ~20 km. The largest slip occurred near the hypocenter, but there is still no consensus on its magnitude, with reported values of ~8 m (Mai et al., 2023) and ~11 m (Goldberg et al., 2023). Likewise, there is still no consensus on the moment magnitude of these two events, but in this study the USGS focal mechanism solutions are considered, which report M_w 7.8 and M_w 7.5 for the Pazarcık and Elbistan earthquakes, respectively (USGS, 2023a, 2023b).

The 2023 Kahramanmaraş sequence produced widespread damage in the built infrastructure and large displacements of population. According to the latest reported information, at least 35,355 buildings fully or partially collapsed, ~180,000 showed heavy damage, ~40,000 presented moderate damage, and almost 430,000 showed evidence of light damage (EERI & GEER, 2023). The EERI/GEER reconnaissance mission report included 11 provinces in Türkiye, covering 3,200 km^2 across the country and the breadth of the damage reasserts the importance of seismic risk quantification. This can be done using the performance-based earthquake engineering (PBEE) framework developed by the Pacific Earthquake Engineering Research (PEER) Center (Cornell & Krawinkler, 2000; Krawinkler & Miranda, 2004). In the PBEE framework, probabilistic seismic hazard analysis (PSHA) and probabilistic seismic demand analysis (PSDA) are integral components (Bozorgnia & Bertero, 2004; Cornell, 2000; Shome et al., 1998). The connection between PSHA and PSDA is the ground motion intensity measure (IM) that provides a way of relating the seismic hazard at the site and the seismic response of the structure.

Among the many possible IMs one could use to describe the ground motion intensity at a site during an earthquake, the most commonly-used one is the 5%-damped pseudo-acceleration spectral ordinate at the fundamental period of vibration of the structure $S_a(T_1)$. However, several researchers have exposed many shortcomings in using S_a as an IM (e.g., Shome, 1999; Baker & Cornell, 2005; Tothong & Luco, 2007; Dávalos & Miranda, 2019a, 2019b;) and in consequence have either proposed modifications to reduce such shortcomings (e.g., Haselton et al., 2011; Mousavi et al., 2011) or have developed new IMs, mostly for structural collapse assessment (e.g., Eads et al., 2015; Kohrangi et al., 2019; Song, 2014; Yakhchalian et al., 2015). Among these novel IMs, Sa_{avg} and $FIV3$ are some of the most promising according to various studies (e.g., Eads et al., 2015; Dávalos and Miranda 2019c, 2020, 2021).

Dávalos and Miranda (2019c) recently introduced $FIV3$, which instead of relying on spectral ordinates, computes the ground motion intensity directly from the ground acceleration history. $FIV3$ is based on fundamental observations by Bertero and his associates on the strong correlation of lateral deformations in structures with the incremental velocity (IV), which they defined as the largest area under individual acceleration pulses between two consecutive zero crossings (Anderson & Bertero, 1987; Bertero et al., 1978, 1976). *FIV3*, proposed by Dávalos and Miranda (2019c, 2020), improved Bertero's *IV* by: (1) using a low-pass filtered acceleration time series to further remove a portion of the high frequency beyond the one removed in conventional record post-processing; (2) integrating not between zero crossings but over a period of time that is a constant fraction of the fundamental period of a structure and therefore, unlike *IV*, *FIV3* becomes period dependent; and (3) instead of focusing on a single pulse, it uses the three largest acceleration pulses with the same polarity to account for ratcheting effects. In short, *FIV3* is computed as the sum of the three largest period-dependent incremental velocities having the same polarity and obtained from a low-pass filtered acceleration time series. A recent thorough examination of the performance of seven different IMs for estimating the collapse risk of several structures (Dávalos & Miranda, 2020, 2021), demonstrated some of the advantages of $FIV3$ in the following categories: (a) efficiency, for collapse intensities it displayed the smallest dispersion; (b) sufficiency with respect to magnitude, source-to-site-distance,

spectral shape, duration, and pulse period; and (c) scaling factor robustness or sufficiency with respect to the scaling factor used when scaling as-recorded ground motions records such as when conducting structural collapse assessments using Incremental Dynamic Analyses (Vamvatsikos & Cornell, 2002). Moreover, the same authors have developed a ground motion model (GMM) (Dávalos et al., 2020) so that a full PSHA and collapse risk assessment can be performed based on $FIV3$ as the IM for structures built on NEHRP site class D and with seismic hazard from shallow crustal earthquakes. However, there are no studies that have examined the directionality of novel IMs such as $FIV3$.

Recently, Poulos and Miranda (2022a) conducted a comprehensive study of the variation of 5%-damped response spectral ordinates with changes in orientation (i.e., azimuth). By using a very large set of ground motions with more than 5,000 record pairs from the NGA-West2 database (Ancheta et al., 2014), they showed that spectral ordinates exhibit a strong directionality and that, on average, maximum response spectral ordinates are, depending on the period, between 36% and 127% higher than those in the perpendicular direction with a tendency of the directionality to increase with increasing period. In a more recent investigation, the same authors showed that the style of faulting has an important influence on directionality and that for strike-slip earthquakes the orientation of maximum response tends to occur in an orientation close to the transverse orientation, which is an orientation perpendicular to that of a line segment between the epicenter and the recording station (Poulos & Miranda, 2023). The possibility of being able to estimate the orientation of maximum intensity suggests that it may be able to anticipate orientations in which current GMM underestimate ground motion intensities and orientations in which they overestimate intensities and therefore eliminate or at least reduce current biased estimates. This could be particularly important not only when evaluating individual structures, but of structures spatially distributed over a region (Heresi & Miranda, 2023) as a large number of structures within a certain urban area could be subjected to ground motions with similar level of directionality and orientation of maximum intensity.

The objective of this paper is to study the directionality of $FIV3$ intensities computed from ground motions recorded during the 2023 Kahramanmaraş earthquake doublet. Both earthquakes in the doublet were well-recorded by over 254 strong-motion recording stations, providing a unique opportunity to study the directionality of ground motions in two large-magnitude strike-slip events. The orientation of maximum $FIV3$ intensity in the horizontal plane is studied in terms of polarization, spatial distribution, and predictability. To this end, the period-dependent parameter, α, proposed by Poulos and Miranda (2023) is used to characterize the directionality and predictability of $FIV3$. To the best of our knowledge, this is the first study that investigates the directionality of $FIV3$, a novel and promising intensity measure for collapse risk assessment.

2. DATASET: EARTHQUAKE GROUND MOTION RECORDS

Strong-motion accelerometer data were obtained from the Turkish Accelerometric Database and Analysis System (TADAS) operated by Turkish Department of Earthquake, Disaster and Emergency Management Authority (AFAD) (AFAD, 2023b, 2023a). This accelerograph network has been operating since 1973 but has been significantly expanded in the last 15 years (Gulkan et al., 2007) and to date comprises 762 individual recording stations countrywide, generating almost 20,000 strong motion records every year (FDSN, 2023). Strong-motion data (raw and processed waveforms) of 379 recording stations were released by AFAD soon after the seismic doublet. We used a carefully selected subset of these stations and the processed version of the strong motion records that was available on early April 2023. The record processing used by AFAD follows the methodology proposed by Paolucci et al. (2011). This processing scheme includes most of the common practices: instrument correction, baseline correction, cosine taper to clip complete recordings, band-pass filtering using a 2nd order acausal frequency-domain Butterworth filter after adding zero-pads at the beginning and end of the signal, among others.

A selection of ground motion records was made following the criteria used by Girmay et al. (2023), which are as follows: (1) using only stations that recorded both horizontal components with reported azimuths of both components; and (2) using only records with a peak ground velocity (PGV) of at least 1 cm/s in one of the recorded horizontal components, aimed at obtaining a strong signal-to-noise ratio over a wide range of periods. Records satisfying these two criteria were used only up to the maximum usable oscillator period (Boore, 2004), defined as 1 over 1.25 times the low-pass corner frequency applied (Abrahamson & Silva, 1997). The latter criterion assures the suitability of the waveform for long-period oscillators. Next, all the records were visually inspected in time and frequency domain to identify anomalies, such as late triggering or incomplete recordings. This selection process resulted in a total of 231 pairs of records from the M_w 7.8 main event and 222 pairs of records from the M_w 7.5 event. The location of the corresponding selected stations is shown in Figure 1 for each of the two events, along with the epicenters and surface projections of the finite fault models proposed by the USGS and projection onto the surface of points of maximum slip within the finite fault models. The USGS finite fault models were also

used to calculate the Joyner-Boore distance (R_{jb}) for each recording station, resulting in a range of distances between 0 and 437 km to the surface projection of the rupture.

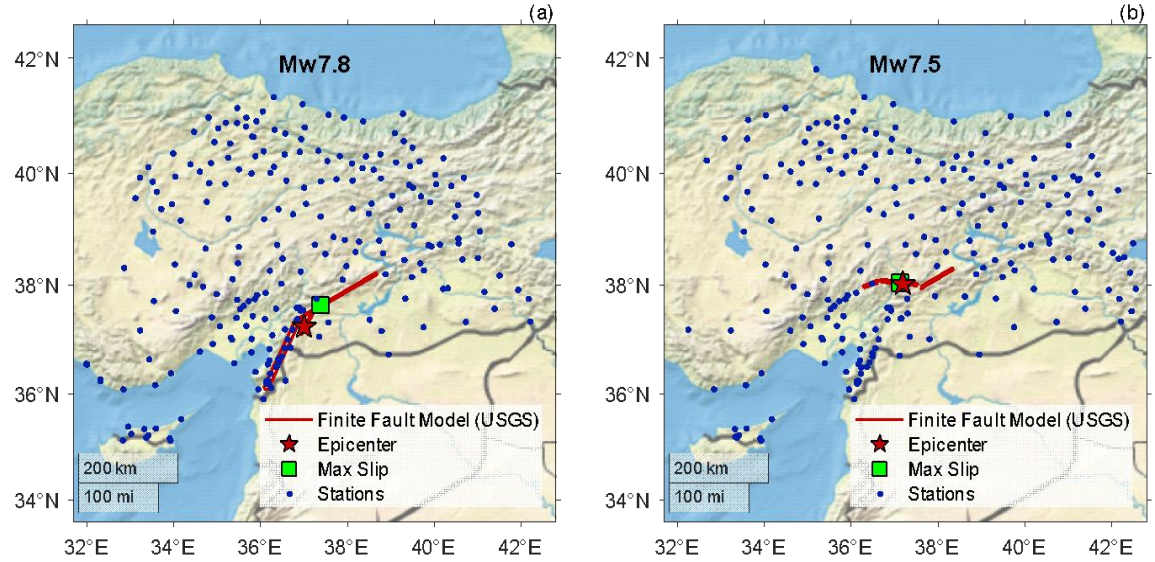

Figure 1. Map of the region of study including the surface projection of the finite fault model proposed by the USGS, the epicenter, the surface projection of the point of maximum slip within the finite fault model, and the selected strong-motion stations that recorded the Kahramanmaraş, Türkiye earthquake doublet: (a) M_w 7.8 event; (b) M_w 7.5 event.

To review the general characteristics and intensities of these events in terms of $FIV3$, Figure 2 presents a comparison between the computed $FIV3$ intensities for a period of vibration of 3 s from the records of both seismic events and the only GMM currently available for this IM, henceforth referred to as DHM2020 (Dávalos et al., 2020). Note that, as DHM2020 was developed for the horizontal arbitrary component, the $FIV3$ of both as-recorded orientations are plotted for each station. As shown in this figure, it can be seen that, in general, the DHM2020 GMM yields a good estimation of $FIV3$ intensities computed from recorded ground motions and of the attenuation trend with increasing distance. The slight overestimation of intensities, particularly for the Mw 7.8 event, can be explained by three reasons. First, the DHM2020 GMM was calibrated only for soil sites classified as NEHRP Class D, that is, stiff soils with mean shear wave velocities in the upper 30 m between 180 m/s and 360 m/s. However, as can be seen in Figure 2, about 60% (i.e., 88 stations) of the selected stations for this study that have a known soil classification, are Class C. And second, the lack of an anelastic attenuation term in DHM2020, which would be reflected by a faster decrease in $FIV3$ intensities at long distances.

Note that, for the main event, there are 12 stations (i.e., 24 horizontal recordings) with an R_{jb} equal to 0, as these stations are over the surface projection of the rupture model. Expectedly, for these stations the GMM overpredicts the intensities since in the original DHM2020 calibration catalogue there was only one record from a strike-slip event with a magnitude over 7.5 and $R_{jb} < 1$ km. These features, coupled with the breadth of the shaking, confirm the significance of these recordings and the long-term vision and adequate planning of the AFAD instrumentation program.

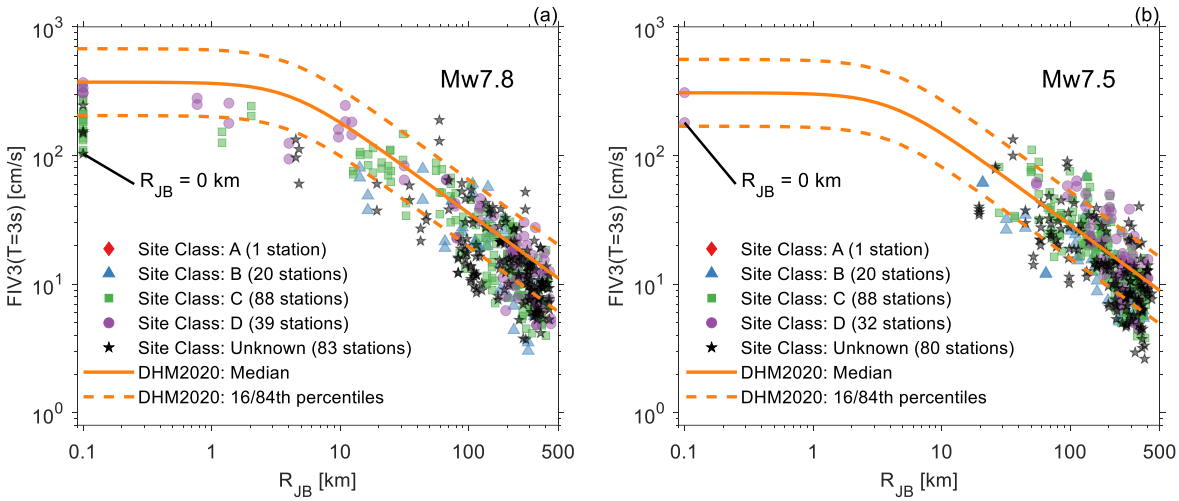

Figure 2. Comparison of *FIV*3 intensities computed from recorded ground motions during the Kahramanmaraş, Türkiye earthquake doublet and the *FIV*3 intensities for the arbitrary component estimated by the DHM2020 model (Site Class D). (a) M_w 7.8 event; (b) M_w 7.5 event.

3. INTRODUCTION OF FIV3 AND GENERAL BEHAVIOR

The intensity measure *FIV3* corresponds to the maximum absolute value of the sum of three incremental velocity values with the same polarity computed from a low-passed filtered acceleration time series. Unlike the original definition of incremental velocity (Bertero et al., 1976; 1978) here the acceleration time history is integrated over durations that correspond to 70% of the period of vibration of the oscillator and therefore *FIV3* is period-dependent. Furthermore, it accounts for the incremental velocity of the three acceleration pulses having the largest incremental velocity and having the same polarity as opposed to focusing only on a single pulse having the largest incremental velocity. Mathematically, *FIV3* is expressed as:

$$FIV3(T_n) = max\{FIV_{max1} + FIV_{max2} + FIV_{max2}, |FIV_{min1} + FIV_{min2} + FIV_{min3}|\} \quad (1)$$

$$FIV(t) = \left\{ \int_t^{t+0.7 \cdot T_n} \ddot{u}_{gf}(\tau) d\tau, \ \forall\, t \right\} \quad (2)$$

where *FIV(t)* is a vector of incremental velocity values computed using time segments with duration $0.7 \cdot T_n$, FIV_{max1}, FIV_{max2}, and FIV_{max3}, are the first, second, and third local maxima incremental velocities in *FIV(t)*, respectively, and similarly, FIV_{min1}, FIV_{min2}, and FIV_{min3}, are the corresponding first, second, and third local minima, respectively. T_n corresponds to the fundamental period of vibration of the structure, and $\ddot{u}_{gf}$ corresponds to the acceleration time series filtered using a 2nd-order Butterworth low-pass filter with a cut-off frequency of 1Hz. Note that term $FIV(t)$ is used herein to refer to the filtered incremental velocity variation in time instead of the original $V_s(t)$ nomenclature used in (Dávalos & Miranda, 2019c, 2020). This was decided to avoid any possible confusion with the commonly used V_s term that refers to the shear wave velocity of a soil stratum.

An example of the computation of *FIV3*, using the ground motion recorded at station 3125 during the M_w 7.8 event is presented in Figure 3. The top subpanel shows the variation in time of the filtered incremental velocity (*FIV*), for a period of 1.5 s. This variation is shown for the orientations at which *FIV*3 is maximum (RotD100), is minimum (RotD00), and one in which it is equal to the median of all non-redundant orientations (i.e., RotD50). Each set of three colored dots corresponds to the three largest values of *FIV* with the same polarity, which added together become the *FIV*3 intensity of each of the three orientations considered. The corresponding values of *FIV*3 are also shown on the upper right corner of the subpanel. The bottom subpanel presents the history of lateral displacement demands of a single-degree-of-freedom (SDOF) system subjected to the RotD00, RotD50, and RotD100 components of the records. The SDOF system has a period of 1.5 s, a critical damping ratio of 5%, a negative post-elastic stiffness ratio of 5%, and a normalized yield strength coefficient, C_y, of 0.15, where C_y is defined as the yield lateral strength normalized by the system's weight. It can be seen that a considerable increase in peak and residual displacement demands is produced with the orientation having the RotD50 intensity as

compared to the demands produced with the ground motions corresponding to the RotD00 component. However, the motion rotated to produce the RotD100 intensity produces dynamic instability in this SDOF, pointing out that strong directionality of $FIV3$ not only can lead to large increments in lateral deformations demands but it can also lead to collapse of structures that could go unnoticed if only RotD50 intensities are used. It should be pointed out that a slight adjustment in the formula used to compute $FIV3$ had to be made in order to avoid spurious large spikes in $FIV3$ at certain orientations of the records. The modification consisted in avoiding the computation of two practically consecutive peaks by adding a window of length $0.7T/dt$ where two peaks should not be simultaneously considered.

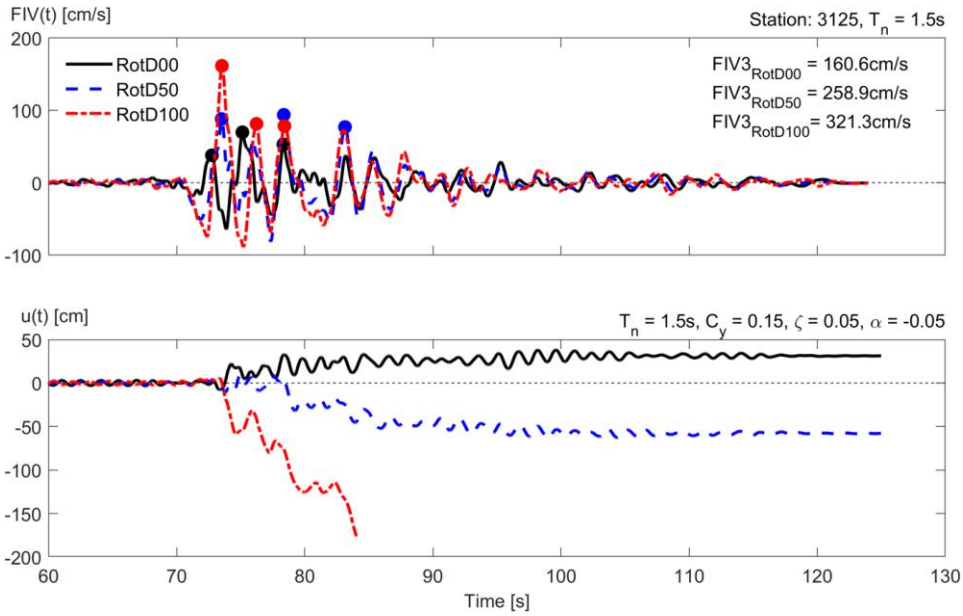

Figure 3. Top: RotD00, RotD50, and RotD100 $FIV3$ time series for a period of 1.5 s, using the strong motions recorded at station 3125 during the M_w 7.8 event. Bottom: Displacement response of a strength-degrading 1.5s, 5%-damped SDOF system with Cy = 0.15 and a post-elastic stiffness of -5% subjected to motions rotated to correspond to the RotD00, RotD50, and RotD100 components of the records.

Figure 4 shows the variation of $FIV3$ intensities for a period of 1.5 s as a function of rotation angle, θ, measured from the EW direction computed using the strong motion records obtained at station 3125 during the M_w 7.8 event. On the left, the variation is presented in a linear fashion whereas the right subfigure uses polar coordinates. Both subfigures present dashed red, dashed blue, and solid black lines representing the $FIV3_{RotD100}$, $FIV3_{RotD50}$, and $FIV3_{RotD00}$ values, respectively. This figure illustrates the strong directionality of $FIV3$ in some of these records. Specifically, in this station the $FIV3$ increases 100% from its minimum (i.e., RotD00) to its maximum value (i.e., RotD100) by rotating the motion 87º, and its maximum value is 23.6% larger than the median intensity from all orientations (i.e., RotD50). This highlights that neglecting directionality by describing the intensity at a site by a single scalar can result in significant underestimations of intensity in certain orientations and significant overestimations in other orientations.

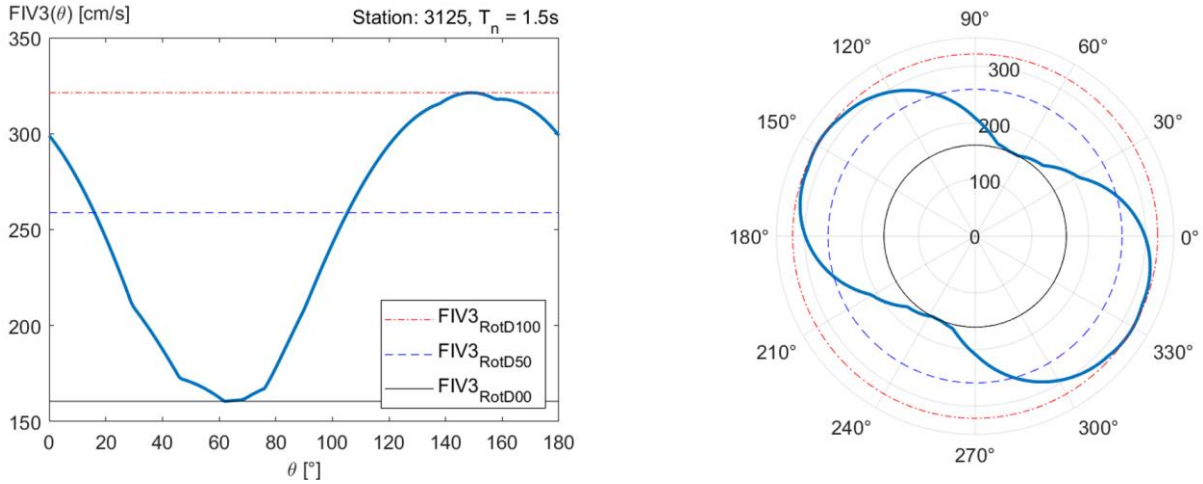

Figure 4. Variation of $FIV3$ with changes in the angle of rotation (measured from the EW direction) for a period of 1.5 s computed with horizontal components recorded at station 3125 during the M_w 7.8 event. Left: linear; and Right: polar representations.

Spectra of $FIV3$ intensities computed from ground motions recorded at stations 2408 and 3125 during the M_w 7.8 event are presented in Figure 5 for six different orientations and for periods ranging from 0.1 to 10 s. It can be seen that, with the exception of very short periods, there is a relatively large variation of $FIV3$ intensities with changes in orientation. Furthermore, it can be observed that for these two stations (and many others as will be demonstrated with results presented in subsequent sections) the $FIV3$ intensities in the transverse orientation (i.e., an orientation perpendicular to the line segment joining the epicenter with the recording station) is very close and for many periods practically equal to the $FIV3$ RotD100 intensities. These results suggest that one may use the transverse direction as a fairly good approximate to determine orientations of maximum intensity. In the following sections, we evaluate the angular difference between the transverse orientation and the RotD100 orientation of $FIV3$ intensities using the parameter α, analogously to what Poulos and Miranda (2023) did when studying the angular difference between the transverse orientation and the orientation of maximum 5%-damped response spectral ordinates.

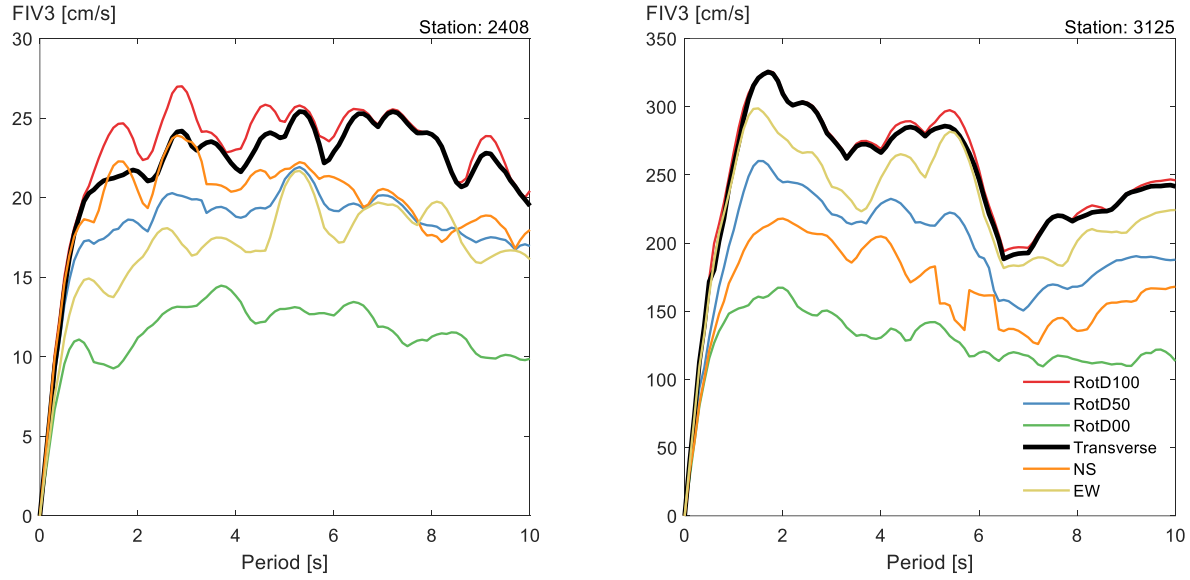

Figure 5. $FIV3$ spectra for six different orientations computed from the strong motions recorded during the M_w 7.8 event. Left: Station 2408; and Right: Station 3125.

Figure 6 presents the ratios of $FIV3$ intensities previously shown in Figure 5. As shown in this figure, the Transverse/RotD100 ratio, shown in a thicker red line is close to unity for practically all the periods, meaning that the transverse direction appears to be a good approximation for the orientation of maximum $FIV3$ intensities, regardless of the period. The transverse-to-radial ratio, shown in a blue line, provides a measure of the level of linear polarization of the records in these two stations, which shows an overall tendency to increase with increasing

period. Considering both stations, the average across all periods is 1.69, indicating that the ground motion intensity is in general significantly larger in the transverse than in the radial direction and reaches a maximum of 2.14 at a period of about 6 s for Station 3125. The RotD100/RotD50 ratio, commonly used in seismic design guidelines (e.g., ASCE/SEI, 2016) to account for directionality in response spectral ordinates is shown in a green line. Averaging the results from both stations, this ratio starts at about 1.14 in the short period region, increases with increasing period, and averages 1.26 across the whole period range.

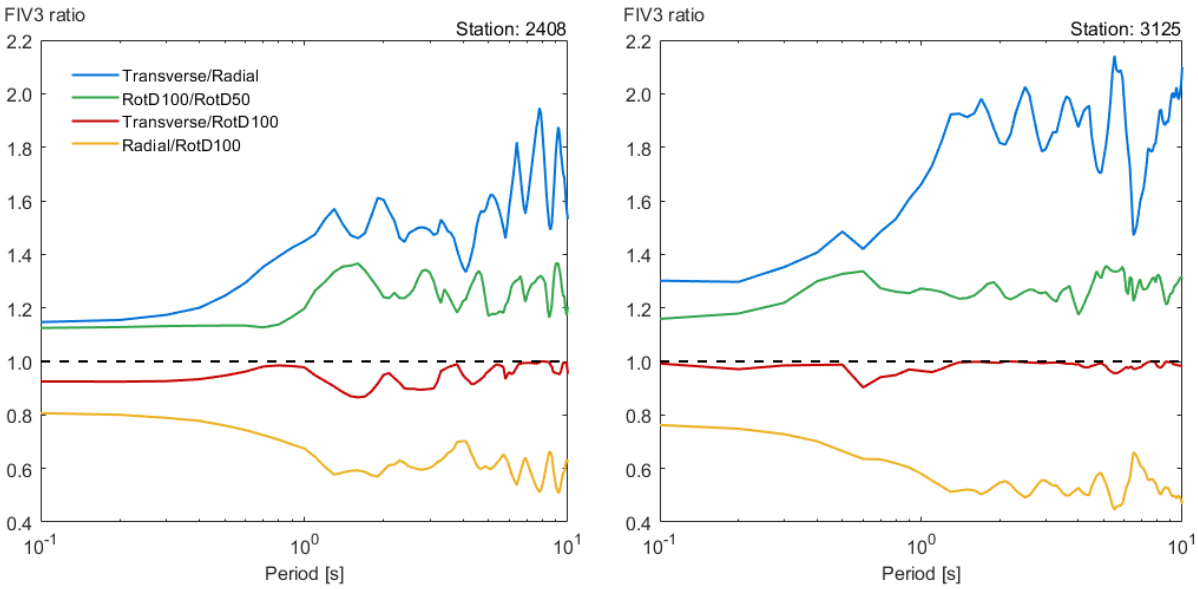

Figure 6. Ratios of $FIV3$ intensities at different orientations as a function of period of vibration computed from ground motions during the M_w 7.8 event recorded at two different stations. Left: Station 2408; and Right: Station 3125.

4. SPATIAL VARIATION OF THE DIRECTION OF MAXIMUM FIV3 INTENSITY

The orientation of the maximum $FIV3$ intensity for a period of 10 s at each station during the Kahramanmaraş earthquake doublet is shown in Figure 7. On each panel, every small circle represents a recording station and the short black lines crossing each circle indicate the orientations of maximum $FIV3$ intensities at each station. The color inside each circle indicates the absolute values of the angular difference between the orientation of maximum $FIV3$ intensity and the transverse orientation, $|\alpha|$, which ranges between 0° and 90°. In particular, Figure 7a presents the spatial distribution of $|\alpha|$ with the transverse orientation computed with respect to the epicenter during the M_w 7.8 event. The first observation is that stations that are near to each other in general exhibit similar orientations of the maximum intensity indicating that, provided that they are not in the close vicinity of the epicenter, all structures within an urban area could experience similar orientations of maximum intensity. A second observation is that the short line segments that indicate the orientations of maximum $FIV3$ intensity exhibit an approximately concentric pattern indicating that the orientations of maximum $FIV3$ intensity tend to occur close to the transverse orientation. A third observation from this figure is that this approximately concentric pattern of the short line segments that indicate the orientations of maximum intensity holds even for long distances from the epicenter, such as 400km. With only a few exceptions, most stations have various tones of blue indicating angular differences of less than 45º. In the lower right corner of each subplot a histogram of this angular difference is shown, which indicates that the orientation of maximum response is far more likely to occur close to the transverse direction and that this likelihood rapidly diminishes as angles approach the radial orientation. In this case the mean value of $|\alpha|$ is 22.31°. Figure 7c shows the geographic distribution of $|\alpha|$ for the M_w 7.5 event and again the transverse directions are computed with respect to the epicenter. In this case, the same observations remain valid for the M_w 7.5 event, but in this case the mean $|\alpha|$ is a slightly higher and equal to 24.8°. These observations are consistent with those made by Poulos and Miranda (2023) for the orientation of maximum 5%-damped spectral ordinates in various strike-slip earthquakes.

The computation of the transverse direction with respect to the epicenter of the event, as originally done by Poulos and Miranda (2023) is one of various ways of computing the transverse orientation. In particular, using the epicenter would be consistent with the use of a point source model originating from the hypocenter. In the discussion section of their manuscript, Poulos and Miranda (2023) commented that ground motions are a

combination of waves originating from different locations on the rupture plane and therefore, if the source-to-site distance is short relative to the rupture length, the transverse orientation could change significantly depending on the location of the rupture segment where larger amplitude waves originate from. In particular, they warned that large-magnitude earthquakes could experience regions of large slip relatively far away from the hypocenter, such as it occurred in the 2002 M_w 7.9 Denali earthquake.

As shown in Figure 1, in the Elbistan M_w 7.5 the epicenter practically coincides with the surface projection of the point of maximum slip in the USGS finite fault model (USGS, 2023a), with the separation between the two points being only 4.8km. However, in the Pazarcik M_w 7.8 the point of maximum slip in the USGS finite fault model (USGS, 2023b) is located approximately 55 km to the northeast of the epicenter. In order to explore if the surface projection of point of maximum slip provides a better point from which to compute the transverse orientation to estimate the orientations of maximum intensity plots, figures similar to 7a and 7c were prepared but now computing the transverse orientations with respect to the surface projection of the point of maximum slip. Results are presented in subpanels 7b and 7d for the M_w 7.8 and 7.5, respectively. It can be seen that, as expected, results for the M_w 7.5 are practically identical whether the transverse direction for computing $|\alpha|$ was done with respect to the epicenter (figure 7c) or with respect to the surface projection of the point of maximum slip (figure 7d), since the two points are nearly collocated for that event. On the other hand, for the much larger M_w 7.8 event, the angular difference $|\alpha|$ is reduced for several stations when computing the transverse orientation with respect to the surface projection of the point of maximum slip (figure 7b) relative to that computed with respect to the epicenter (figure 7a). This results in a slight reduction in the mean $|\alpha|$ from 22.31º to 19.54º, representing a 12.4% reduction. In other words, the predictability of the direction of maximum FIV3 intensity increases if the surface projection of the maximum slip point is considered as the seismic source instead of the epicenter. These results are consistent with those found by Girmay et al. (2023) who also explored the use of the surface projection of the point of maximum slip for estimating the direction of maximum 5%-damped response spectral ordinates during the 2023 Türkiye earthquake doublet.

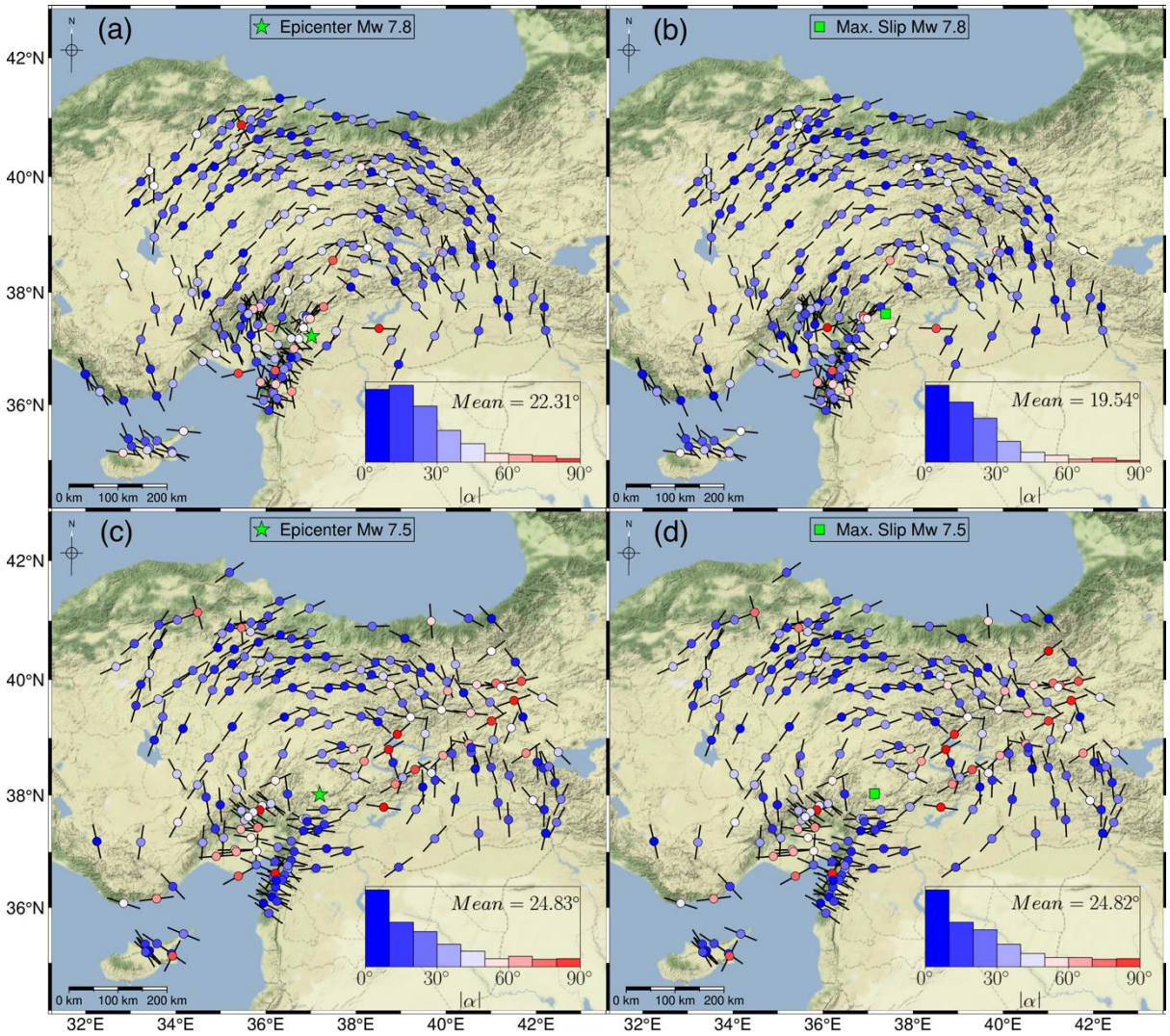

Figure 7. Orientation of maximum $FIV3$ intensities for a period of vibration of 10 s during the M_w 7.8 (panels a and b) and M_w 7.5 (panels c and d) events and their angular difference with respect to the transverse orientation. Black crossing lines correspond to the orientation of the maximum intensity and the color indicates the angular difference to the transverse orientation (α). The bottom right insert on each map corresponds to the histogram and the mean $|\alpha|$ along with the color-based intensity. The computation of $|\alpha|$ is shown with respect to the epicenter (panels a and c) and with respect to the surface projection point of maximum slip (panels b and d) for both events, respectively.

It should be noted that the precise orientation of the direction of maximum intensity is not necessary because, as shown by Poulos and Miranda (2022a), intensity variations within $\pm 25^{o}$ are typically less than 10% from that of the RotD100 intensity.

5. SPATIAL VARIATION OF THE POLARITY AND DIRECTIONALITY OF FIV3 INTENSITIES

The predictability of the approximate orientation of the maximum intensity of a ground motion in the horizontal plane in strike-slip earthquakes has important implications in engineering practice. For example, this might pave the way for the development of orientation-specific ground motion models that provide improved estimates of ground motion intensity. For example, Poulos and Miranda (2022b) have recently shown that there are probabilities between 92% and 98% of exceeding the 5%-damped RotD50 response spectral ordinate in one of the two principal axes of a structure (which are generally orthogonal with respect to each other). However, it is important to assess how larger the RotD100 $FIV3$ intensities are with respect to the RotD50 FIV3 intensities (whose median could be estimated, for example, with the currently available DHM2020 GMM) and their spatial distribution in large magnitude strike-slip earthquakes. Therefore, it is needed to study first the relationship between the maximum intensity (i.e., RotD100) and the central tendency (i.e., RotD50 in this case) and second the relation between the intensity at the transverse orientation (i.e., $FIV3_T$) and RotD50 along with their spatial distributions during large-magnitude strike-slip earthquakes.

Figure 8 shows the spatial distribution of the RotD100/RotD50 ratio of the $FIV3$ intensities for a period of 10 s for both the M_w 7.8 Pazarcık and M_w 7.5 Elbistan events. As shown in this figure, this ratio displays a similar average behavior for both events in terms of their geographic distribution as well as their mean ratio averaged over all stations in each event, with the latter being virtually identical and equal to ~1.24 for both events in the doublet. Again, circles correspond to each recording station and the color inside them indicates the RotD100/RotD50 ratio of the $FIV3$ intensities at each site. As indicated in these figures, most ratios are larger than 1.2 and this is true for stations close to the source as well as for stations that are more than 300 km from the source. Also noticeably is that the histograms of the ratio (shown at the bottom right corners of each subpanel), present very similar distributions, significantly departing from a uniform distribution and are skewed towards higher ratios. Similarly to what occurs with response spectral ordinates, and as first pointed out by Boore for that measure of intensity (Boore, 2010), the upper limit of this ratio is also $\sqrt{2}$, which corresponds to the ratio of a fully linearly polarized ground motion.

Maps similar to those of figure 8, but now for the spatial distribution of the ratio between the $FIV3$ intensity in the transverse component and the RotD50 $FIV3$ intensity for the same period of 10 s are shown in Figure 9. Since the transverse orientation depends on the seismic source location, the results are presented both with respect to the epicenter (panels a and c) and with respect to the surface projection of the point of maximum slip in the USGS finite fault model (panels b and d). The first remark is that, regardless of the earthquake event or of the point considered to compute the transverse orientation, the distribution and mean of the $FIV3_T/FIV3_{RotD50}$ ratios are spatially similar with a similar mean value ranging from 1.14 to 1.17, and having a strongly skewed probability distribution towards values higher than 1.2, with many values approaching the upper limit (i.e., $\sqrt{2}$). Secondly, since the maximum intensity tends to occur close to the transverse orientation (see Figure 7), the $FIV3$ intensity at the transverse orientation is, for practically all stations, well above the RotD50 $FIV3$ intensity. Even more, in some regions, such as in the subset of 25 almost in-line red-colored stations located south-west of the epicenter of the M_w 7.5 event near the Amanos segment of the EAF, the mean ratio between the transverse intensity and RotD50 intensity reaches a value of 1.23. This indicates that in these regions close to the fault, $FIV3$ intensities in the transverse orientation were, on average, 23% larger than the median intensity from all orientations.

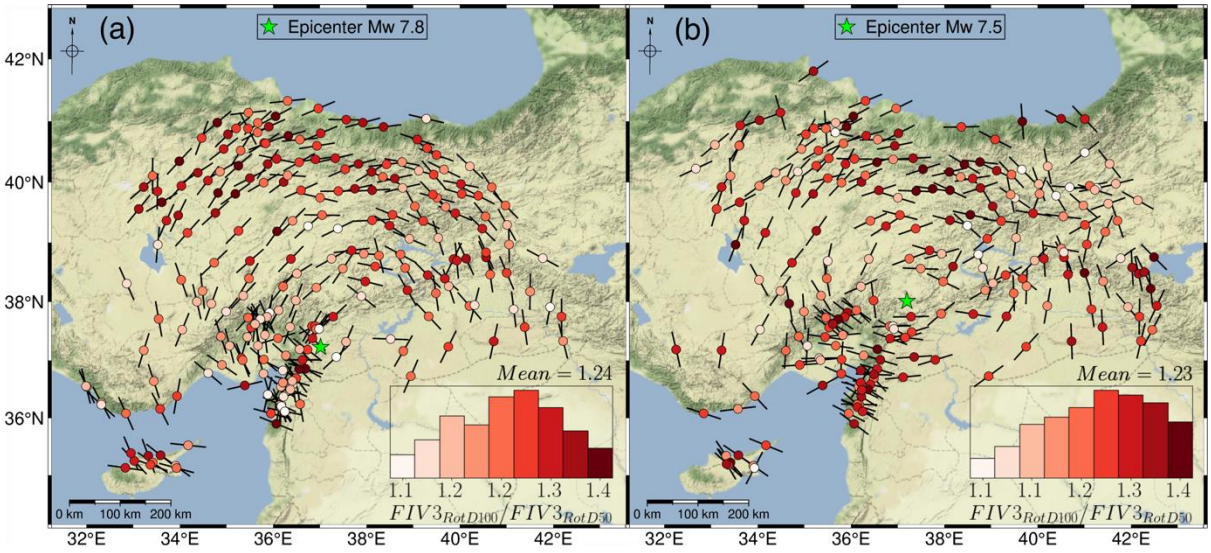

Figure 8. Spatial distribution and empirical probability distribution of $FIV3_{RotD100}$ to $FIV3_{RotD50}$ ratios computed for a period of 10 s, for (a) M_w 7.8; and (b) M_w 7.5 events.

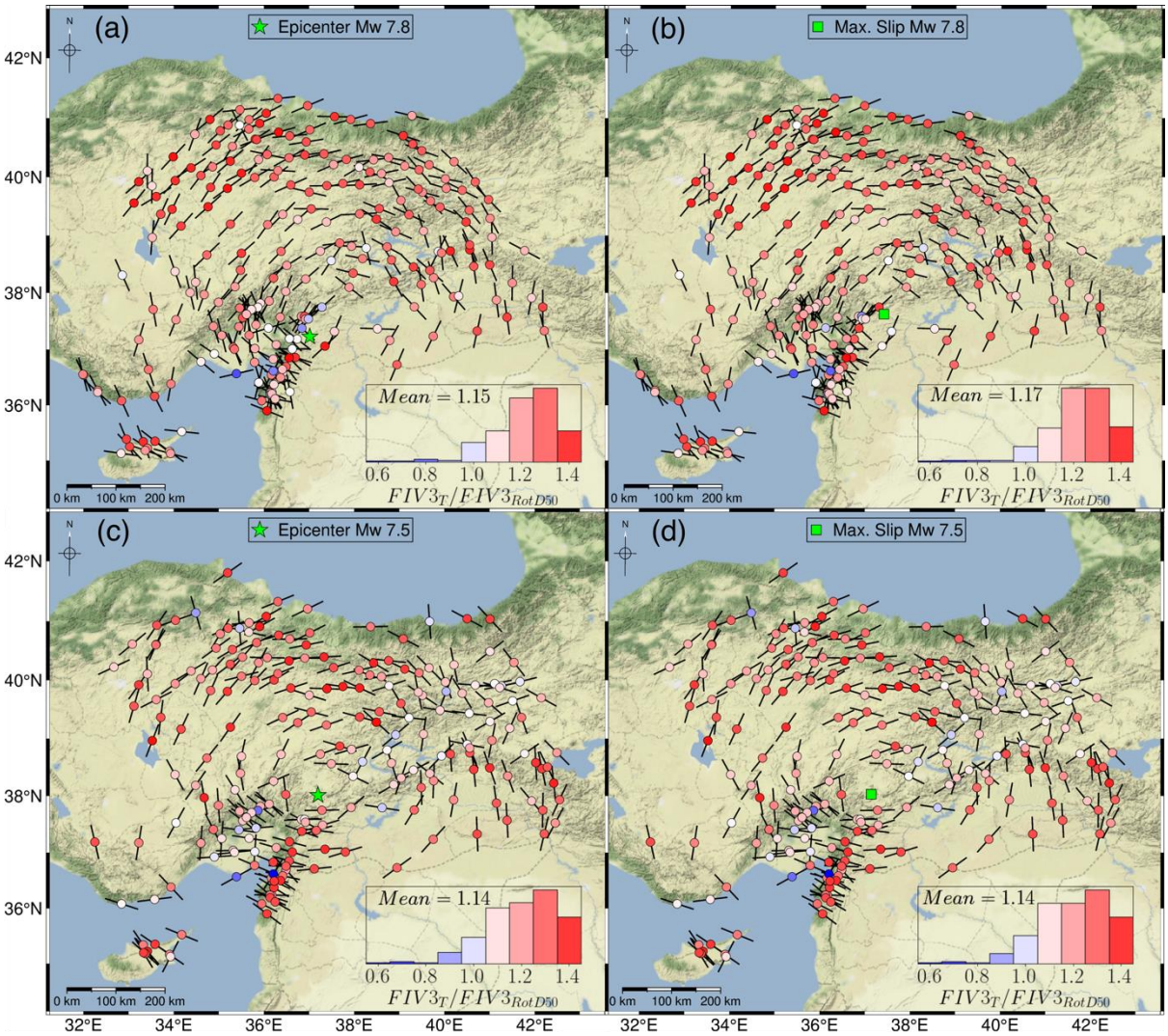

Figure 9. Spatial distribution and empirical probability distribution of $FIV3_T$ to $FIV3_{RotD50}$ ratios computed for a period of 10 s, for the M_w 7.8 (panels a and b) and M_w 7.5 (panels c and d) earthquakes. The transverse orientation

is computed with respect to the epicenter in panels a and c) and with respect to the surface projection of the point the maximum slip in panels b and d.

Figures ES1 to ES12 in the electronic supplement of this manuscript present the same information shown in figures 7, 8, and 9, but for periods of vibration of 1 s, 3 s, 5 s, and 7 s in order to observe the extent of polarization for shorter periods of vibration.

Another way to examine the intensity at the transverse orientation is by taking advantage of the readily available DHM2020 GMM. Although the predicted intensity of this GMM, as explained earlier, is the arbitrary component of the horizontal recordings, this GMM can be used to investigate if systematic deviations (i.e., offsets) exist when considering other orientations. To this end, Figure 10 shows the variation of total residuals, ε (i.e., between-event plus within-event), computed using the DHM2020 predictions and the transverse component $FIV3$ intensities computed with respect to the epicenter and RotD50 at every station for a period equal to 3 s for the M_w 7.8 main event. Figure 10a shows that residuals in practically all stations are larger in the transverse component than when using the RotD50 intensities across all Joyner-Boore distances, R_{JB}. Moreover, the mean of ε for all stations, shown in the histogram in Figure 10b, is systematically larger for the transverse component by 21%. This behavior was observed in both earthquake events and for all periods considered.

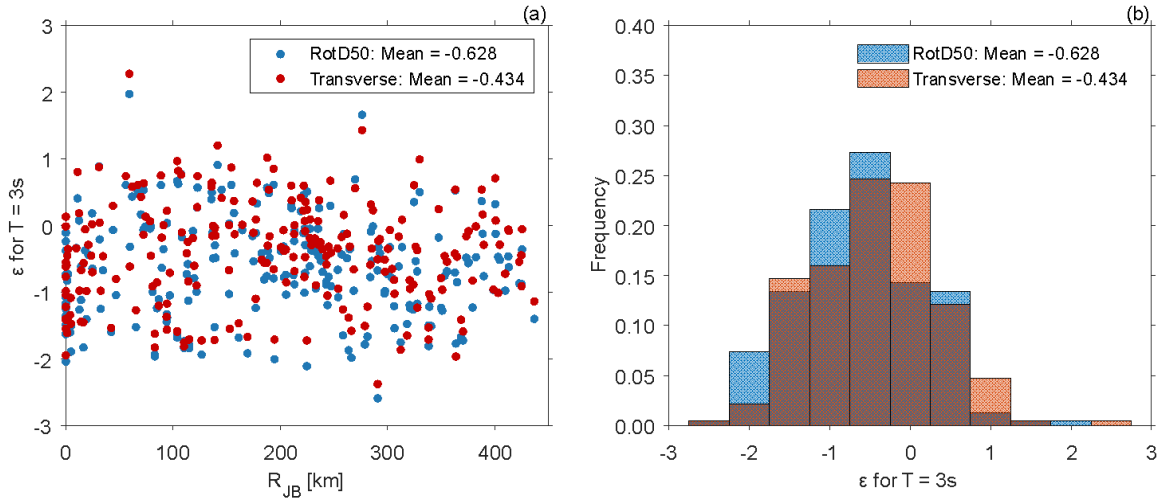

Figure 10. (a) Variation of residuals ε of $FIV3$ with respect to intensities estimated using DHM2020 for a period of 3 s as a function of Joyner-Boore distance, R_{JB}; (b) histogram of ε values for $FIV3$ for a period of 3 s. In both cases, ε values are computed with the RotD50 intensity (in blue) and the intensity at the transverse orientation with respect to the epicenter (in red) for each station during the M_w 7.8 main event.

To further evaluate the $FIV3$ directionality of different ground motions during the 2023 Kahramanmaraş earthquake doublet, including a wider range of vibration periods, two normalized orientation-dependent parameters are introduced. The first parameter is $\eta(\phi)$, used initially by Hong and Goda (2007) to study the change of pseudo-acceleration spectral ordinates at different orientations as rotations departs from the orientation of maximum intensity. This ratio is now used in this study to assess the directionality of $FIV3$, as shown in Equation 3, where $FIV3(\phi)$ is the $FIV3$ intensity at an orientation with an angle of ϕ with respect to the orientation of the maximum $FIV3$ intensity, and $FIV3_{RotD100}$ is the RotD100 $FIV3$ intensity. Note that, by definition, i.e., $FIV3(\phi = 0)$ corresponds to the RotD100 intensity and thus, $\eta(\phi = 0) = 1$. The second ratio is $\nu(\phi)$, similar to $\eta(\phi)$, but, as shown in Equation 4, the normalization in this case is now done with respect to RotD50 (Poulos & Miranda, 2023). The usefulness of these ratios is that they allow us to compute intensities at any angle of rotation by using the maximum or median intensity, with the latter frequently estimated by GMMs, so as the median for the arbitrary component in the DHM2020 GMM for $FIV3$ which is essentially the same as the median of RotD50 of $FIV3$.

$$\eta(\phi) = \frac{FIV3(\phi)}{FIV3_{RotD100}} \qquad (3)$$

$$\nu(\phi) = \frac{FIV3(\phi)}{FIV3_{RotD50}} \qquad (4)$$

To compute $\eta(\phi)$ and $\nu(\phi)$ ratios, the 231 pairs of horizontal ground motions recorded during the M_w 7.8 event were used. Since $FIV3(\phi)$ repeats itself every 180° (see Figure 4b), the angle ϕ ranges from -90° to +90° and the ratios were computed every 0.5°. However, ϕ is going to be shown from 0° to 90° due to symmetry. Two statistics are used to present the results, namely the geometric mean of the ratios, μ_η and μ_ν, as well as the standard deviations of $ln\,\eta$ and $ln\,\nu$, $\sigma_{ln\,\eta}$ and $\sigma_{ln\,\nu}$, which are shown in Figure 11. Figure ES13 in the supplement has the corresponding information for the M_w 7.5 event. Regarding η, the first observation is that for all periods of vibration, the geometric mean of η decreases monotonically as the rotation angle, ϕ, increases, somewhat faster in the first 45° and more gradually afterwards to reach a plateau around 90°. The second remark is that the longer the period, the larger the reduction in intensity as the orientation is rotated away from the orientation of maximum $FIV3$ intensity, that is, similarly to response spectral ordinates, $FIV3$ also tends to become more linearly polarized as the period increases. There is also a monotonic decrease in the geometric mean of ν for all periods as ϕ increases, with a similar inflection point around 45°. For rotation angles smaller than about 45º the geometric mean of ν is larger than 1, hence the $FIV3(\phi)$ intensity is, on average, larger than the RotD50 intensity. Conversely, for rotation angles larger than ~45°, $FIV3(\phi)$ is lower than RotD50, with more significant reductions in intensity for longer periods of vibration. Remarkably, the shapes of μ_η and μ_n are very similar to those reported by Poulos and Miranda (2022a) for 5%-damped response spectral ordinates, S_a, even though the computation of $FIV3$ intensities does not involve peak responses of linear elastic oscillators. Regarding the standard deviation of the logarithmic ratio, $\sigma_{ln\,\eta}$, which is a quantitative measure of the record-to-record variability of the η ratio, it increases monotonically for all periods of vibration as the rotation angle ϕ departs from the orientation of maximum $FIV3$ intensity. For rotation angles smaller than about 50°, the standard deviation is similar for all periods, except for the shortest period (i.e., 0.1 s) that exhibits a slightly larger magnitude with a stepwise shape, which might be explained by the small number of records used to compute these statistics. Beyond 50°, the standard deviation increases faster for longer periods of vibration, reaching a maximum of 0.3 for a period of 10 s. Although the overall trend is similar to that reported by Poulos and Miranda (2022a) for S_a, it should be noted that maximum variabilities of intensities at an orientation perpendicular to the orientation of maximum intensity are 40% lower for $FIV3$ than for S_a. For rotation angles smaller than ~50°, the logarithmic standard deviation of ν is very small and stable around 0.07, irrespective of the vibration period, suggesting a quasi-deterministic estimation of this ratio could suffice for many engineering applications for rotation angles less than ~50°. After that, $\sigma_{ln\,\nu}$ increases with increasing period, however the largest value for $\phi = 90°$ equals to 0.24 and at a period equal to 10 s is still about 45% lower than the variability reported by Poulos and Miranda (2022a) for S_a. These relatively low dispersions on the η and ν parameters, when compared with those reported on the DHM2020 GMM for the arbitrary component of *FIV3* conditioned on causal parameters, mean that uncertainty in the estimation of *FIV3* intensities at specific orientations would be very similar to those of RotD50 $FIV3$ intensities.

To further understand the directionality of $FIV3$ intensities and their variation with changes in the period of vibration, Figure 12a shows the median of a set of $FIV3$ ratios of interest at different orientations for the M_w 7.8 earthquake while Figure 12b shows the same ratios for the M_w 7.5 event. In both cases $FIV3$ ratios were computed for 12 periods of vibration between 0.1 and 10 s and considering all recording stations. The first observation is that for this sequence of strike-slip earthquakes, the intensity at the transverse orientation is significantly larger than the intensity at the radial component, with a stable ratio of 1.18 for periods shorter than 1 s and increasing monotonically afterwards up to 1.5. In other words, the larger the period, the larger the linear polarization of the ground motion intensity from the radial orientation towards the transverse component. Second, the ratio between the maximum intensity, RotD100, and the median intensity, RotD50 is very stable across all periods, ranging between 1.16 and 1.23. Third, the ratio between the intensity at the transverse orientation and RotD50 is, like the previous ratio, very stable across all periods, ranging between 1.05 and 1.15. Fourth, the ratio between the intensity at the transverse orientation and RotD100 is slightly larger than 0.9 and flat across all periods. Fifth, the ratio between the intensity at the radial component and RotD100 decreases monotonically as the period increases, ranging from 0.78 at 0.1 s to 0.6 at 10 s. Noticeably, all these observations are valid for both earthquakes. For periods smaller than about 2 s, the directionality of $FIV3$ intensities is larger than that reported by Girmay et al. (2023) for response spectral ordinates for the same doublet considered herein. Finally, some of these ratios, such as the intensity at the transverse orientation and RotD50 could be used to generate correction factors for DHM2020 GMM to yield accurate ground motion intensity measures at the transverse orientation.

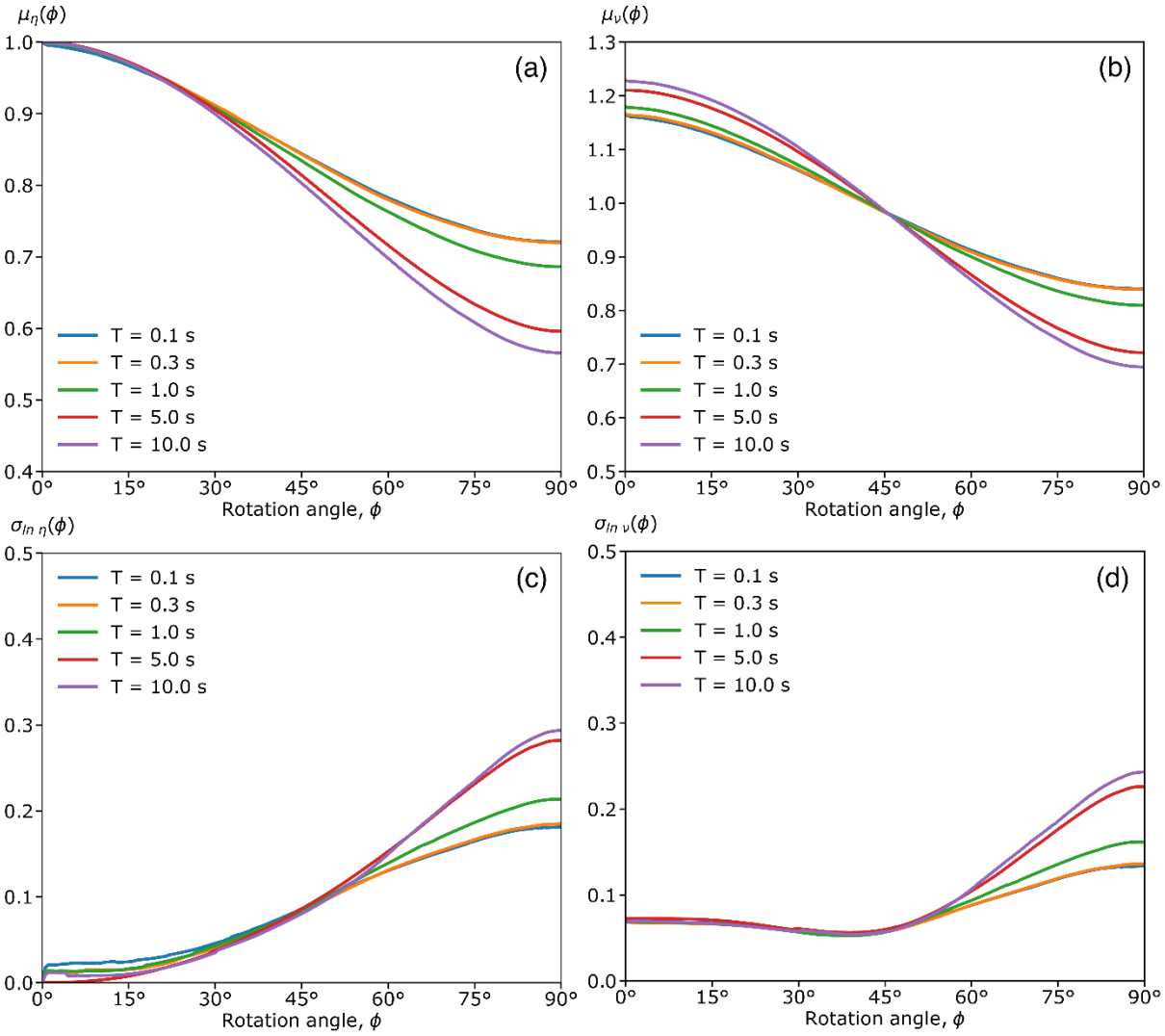

Figure 11. Geometric mean of (a) η and (b) ν ratios and standard deviation of (c) $ln\ \eta$ and (d) $ln\ \nu$ for 5 different periods. Dataset: Earthquake M_w 7.8 ground motion records.

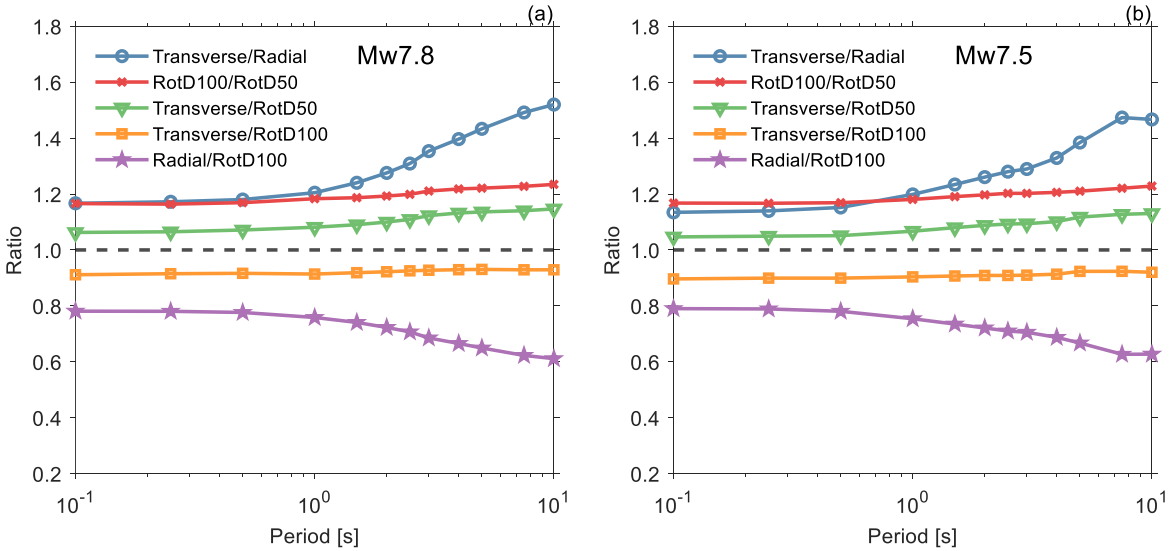

Figure 12. Median ratios of *FIV*3 intensities at different orientations as a function of period of vibration, during the Kahramanmaraş, Türkiye earthquake doublet: (a) M_w 7.8 event; (b) M_w 7.5 event.

6. SUMMARY AND CONCLUSIONS

The directionality of $FIV3$ ground motion intensities has been investigated for the first time. The study was conducted by using a large set of strong ground motions recorded during the February 6, 2023, M_w 7.8 Pazarcık and M_w 7.5 Elbistan earthquake doublet, to date the best recorded doublet of large-magnitude strike-slip events. The orientation of the maximum response of $FIV3$ in the horizontal plane was carefully examined along with its spatial distribution and the level of linear polarization was evaluated by using ratios of intensities at different orientations.

$FIV3$ intensities exhibited a strong directionality across most of the ground motions recorded during both earthquake events and this was found to occur not only for stations located in the near-rupture field but also for stations located at large Joyner-Boore distances such as 400 km. The orientation of the maximum $FIV3$ intensity was systematically close to the transverse direction, that is, an orientation perpendicular to the line segment between the epicenter and the recording strong motion station. This orientation of maximum $FIV3$ intensity is consistent to that previously observed and documented by Poulos and Miranda (2023) for 5%-damped pseudo acceleration response spectral ordinates, S_a, when using strike-slip earthquake records gathered from the NGA-West2 ground motion database.

For the M_w 7.8 Pazarcık event, where the surface projection of the point of maximum slip inferred from the USGS finite fault model of the earthquake was located approximately 55 km away from the epicenter, it was found that computing the transverse orientation by using the surface projection of the point of maximum slip leads to slightly better estimates of the orientation of the maximum $FIV3$ intensity. Meanwhile, for the M_w 7.5 Elbistan event, where the surface projection of the point of maximum slip inferred from the USGS finite fault model of the earthquake is just ~4.8 km away from the epicenter, practically the same results are obtained whether the transverse orientation is computed using the epicenter or the surface projection of the point of maximum slip. These results are consistent with those recently found by Girmay et al. (2023) for the 5%-damped pseudo acceleration response spectral ordinates for this 2023 Turkish earthquake doublet.

The variation of $FIV3$ intensities with rotations away from the orientation of maximum intensity, ϕ, as measured by the geometric means of non-dimensional ratios $\eta(\phi)$ and $\nu(\phi)$, was found to be remarkably similar to the variation previously reported by Poulos and Miranda (2022a) for 5%-damped pseudo acceleration response spectral ordinates. However, the dispersions of $\eta(\phi)$ and $\nu(\phi)$ for $FIV3$ intensities and rotation angles larger than 50º were found to be significantly lower than those reported for S_a, indicating that the directionality of $FIV3$ is more predictable that of S_a. However, further studies should be conducted to verify if this holds true across a larger number of seismic events having a wide range of magnitudes, source-to-site distances, and faulting mechanisms.

The $FIV3$ intensities estimated for these two events using the DHM2020 GMM were found to provide, in general, good estimates of observed intensities despite being based on a ground motion database that contained only a small number of records of large-magnitude strike-slip events. For the M_w 7.5 Elbistan event, the estimated $FIV3$ intensities were particularly good, whereas for the M_w 7.8 Pazarcık event, the GMM slightly overestimated the observed $FIV3$ intensities. Close examination of the spatial distribution of $FIV3$ intensities in the transverse orientation indicates that for most stations, the corresponding intensities are between 15% to 40% higher than the median $FIV3$ intensities across all orientations (i.e., RotD50 $FIV3$ intensities). These results, together with those presented by Girmay et al. (2023) indicate that it is possible in the future to develop orientation-specific GMMs that provide improved estimates of ground motion intensities as a result of strike-slip earthquakes that are of primary concern to seismic regions such as Türkiye or California. In particular, the development of such GMMs for $FIV3$ would be an important contribution as this ground motion intensity measure outperforms many other intensity measures in terms of efficiency, sufficiency, predictability, and scaling factor robustness for estimating seismic structural collapse within the PBEE framework.

7. ACKNOWLEDGMENTS

The authors are grateful to the Turkish Disaster and Emergency Management Authority (AFAD) for installing and maintaining the strong motion seismic instrumentation network in Türkiye and for collecting, processing and distributing the strong motion records soon after the earthquake events. This study would have not been possible without these records. The authors would also like to thank Dr. M. Abdullah Sandikkaya and Dr. Sinan Akkar for the information they provided on the strong motion recordings in the Türkiye earthquakes. The authors are also grateful to Nathan Girmay and Alan Poulos, PhD students at Stanford University for their assistance in the

selection of ground motions used in this study. Similarly, the authors acknowledge Arnoldo Andrade from Universidad Panamericana for coding and post-processing some of the preliminary results used in this manuscript. The second author would like to thank the financial support of the ANID FONDECYT Iniciación en Investigación Project #11230463. Finally, the authors would like to thank the three anonymous reviewers, whose comments and suggestions significantly improved the quality of this paper.

8. REFERENCES

Abrahamson, N. A., & Silva, W. J. (1997). Empirical response spectral attenuation relations for shallow crustal earthquakes. *Seismological Research Letters*, *68*(1), 94–127.

AFAD. (2023a). *Turkish Disaster and Emergency Management Presidency (AFAD) Elbistan (Kahramanmaraş) Earthquake MW 7.5*. Available from: Https://Tadas.Afad.Gov.Tr/Event-Detail/17969 (Accessed April 2023).

AFAD. (2023b). *Turkish Disaster and Emergency Management Presidency (AFAD) Pazarcık (Kahramanmaraş) Earthquake Mw 7.7*. Available from: Https://Tadas.Afad.Gov.Tr/Event-Detail/17966 (Accessed April 2023).

Ambraseys, N. N. (1989). Temporary seismic quiescence: SE Turkey. *Geophysical Journal International*, *96*(2), 311–331.

Ancheta, T. D., Darragh, R. B., Stewart, J. P., Seyhan, E., Silva, W. J., Chiou, B. S.-J., Wooddell, K. E., Graves, R. W., Kottke, A. R., Boore, D. M., & others. (2014). NGA-West2 database. *Earthquake Spectra*, *30*(3), 989–1005.

Anderson, J. C., & Bertero, V. V. (1987). Uncertainties in establishing design earthquakes. *Journal of Structural Engineering*, *113*(8), 1709–1724.

ASCE/SEI. (2016). *Minimum design loads and associated criteria for buildings and other structures*. ASCE/SEI 7-16, American Society of Civil Engineers, Reston, VA.

Baker, J. W., & Cornell, A. (2005). A vector-valued ground motion intensity measure consisting of spectral acceleration and epsilon. *Earthquake Engineering & Structural Dynamics*, *34*(10), 1193–1217.

Bertero, V. V, Herrera, R. A., & Mahin, S. A. (1976). Establishment of design earthquakes—Evaluation of present methods. *Proc., Int. Symp. on Earthquake Structural Engineering*, *1*, 551–580.

Bertero, V. V, Mahin, S. A., & Herrera, R. A. (1978). Aseismic design implications of near-fault San Fernando earthquake records. *Earthquake Engineering & Structural Dynamics*, *6*(1), 31–42.

Boore, D. M. (2004). *Choosing the Lowest Usable Frequency for Response Spectra from Filtered Data*. http://www.daveboore.com/daves_notes/lowest_usable_freq_for_response_spectra_v20.pdf

Boore, D. M. (2010). Orientation-independent, nongeometric-mean measures of seismic intensity from two horizontal components of motion. *Bulletin of the Seismological Society of America*, *100*(4), 1830–1835.

Bozorgnia, Y., & Bertero, V. V. (2004). *Earthquake engineering: from engineering seismology to performance-based engineering*. CRC press.

Cornell, A. (2000). Progress and challenges in seismic performance assessment. *PEER Newsletter*.

Cornell, A., & Krawinkler, H. (2000). *Progress and challenges in seismic performance assessment. PEER Center News, Spring 2000*.

Dal Zilio, L., & Ampuero, J.-P. (2023). Earthquake doublet in Turkey and Syria. *Communications Earth & Environment*, *4*(1), 71.

Dávalos, H., Heresi, P., & Miranda, E. (2020). A ground motion prediction equation for filtered incremental velocity, FIV3. *Soil Dynamics and Earthquake Engineering*, *139*, 106346.

Dávalos, H., & Miranda, E. (2019a). Evaluation of bias on the probability of collapse from amplitude scaling using spectral-shape-matched records. *Earthquake Engineering & Structural Dynamics*, *48*(8), 970–986.

Dávalos, H., & Miranda, E. (2019b). Evaluation of the scaling factor bias influence on the probability of collapse using Sa(T1) as the intensity measure. *Earthquake Spectra*, *35*(2), 679–702.

Dávalos, H., & Miranda, E. (2019c). Filtered incremental velocity: A novel approach in intensity measures for seismic collapse estimation. *Earthquake Engineering & Structural Dynamics*, *48*(12), 1384–1405.

Dávalos, H., & Miranda, E. (2020). Evaluation of FIV3 as an intensity measure for collapse estimation of moment-resisting frame buildings. *Journal of Structural Engineering*, *146*(10), 4020204.

Dávalos, H., & Miranda, E. (2021). Robustness evaluation of FIV3 using near-fault pulse-like ground motions. *Engineering Structures*, 230, 111694.

Eads, L., Miranda, E., & Lignos, D. (2016). Spectral shape metrics and structural collapse potential. *Earthquake Engineering & Structural Dynamics*, *45*(10), 1643–1659.

Eads, L., Miranda, E., & Lignos, D. G. (2015). Average spectral acceleration as an intensity measure for collapse risk assessment. *Earthquake Engineering & Structural Dynamics*, *44*(12), 2057–2073.

EERI, E. E. R. I., & GEER, G. E. E. R. (2023). *February 6, 2023 Türkiye Earthquakes: Report on Geoscience*

and Engineering Impacts. https://doi.org/10.18118/G6PM34
Emre, Ö., Duman, T. Y., Özalp, S., Şaroğlu, F., Olgun, Ş., Elmacı, H., & Ça, T. (2018). Active fault database of Turkey. *Bulletin of Earthquake Engineering*, *16*(8), 3229–3275.
FDSN. (2023). *International Federation of Digital Seismograph Networks*. Https://Www.Fdsn.Org/Networks/Detail/TK/.
Girmay, N., Poulos, A., & Miranda, E. (2023). Directionality and Polarization of Response Spectral Ordinates in the 2023 Kahramanmaras, Türkiye Earthquake Doublet. *Submitted to Earthquake Spectra*.
Goldberg, D. E., Taymaz, T., Reitman, N. G., Hatem, A. E., Yolsal-Çevikbilen, S., Barnhart, W. D., Irmak, T. S., Wald, D. J., Öcalan, T., Yeck, W. L., & others. (2023). Rapid Characterization of the February 2023 Kahramanmaraş, Türkiye, Earthquake Sequence. *The Seismic Record*, *3*(2), 156–167.
Gülerce, Z., Shah, S. T., Menekşe, A., Özacar, A. A., Kaymakci, N., & Çetin, K. Ö. (2017). Probabilistic seismic-hazard assessment for East Anatolian fault zone using planar fault source models. *Bulletin of the Seismological Society of America*, *107*(5), 2353–2366.
Gulkan, P., Ceken, U., Colakoglu, Z., Ugras, T., Kuru, T., Apak, A., Anderson, J. G., Sucuoğlu, H., Çelebi, M., Akkar, D. S., & others. (2007). Enhancement of the national strong-motion network in Turkey. *Seismological Research Letters*, *78*(4), 429–438.
Haselton, C. B., Baker, J. W., Liel, A. B., & Deierlein, G. G. (2011). Accounting for ground-motion spectral shape characteristics in structural collapse assessment through an adjustment for epsilon. *Journal of Structural Engineering*, *137*(3), 332–344.
Heresi, P., & Miranda, E. (2023). RPBEE: Performance-based earthquake engineering on a regional scale. *Earthquake Spectra*, 87552930231179490.
Hong, H. P., & Goda, K. (2007). Orientation-dependent ground-motion measure for seismic-hazard assessment. *Bulletin of the Seismological Society of America*, *97*(5), 1525–1538.
Kohrangi, M., Vamvatsikos, D., & Bazzurro, P. (2019). Pulse-like versus non-pulse-like ground motion records: spectral shape comparisons and record selection strategies. *Earthquake Engineering & Structural Dynamics*, *48*(1), 46–64.
Krawinkler, H., & Miranda, E. (2004). Performance-based earthquake engineering. *Earthquake Engineering: From Engineering Seismology to Performance-Based Engineering*, *9*, 1–9.
Mai, P. M., Aspiotis, T., Aquib, T. A., Cano, E. V., Castro-Cruz, D., Espindola-Carmona, A., Li, B., Li, X., Liu, J., Matrau, R., & others. (2023). The Destructive Earthquake Doublet of 6 February 2023 in South-Central Türkiye and Northwestern Syria: Initial Observations and Analyses. *The Seismic Record*, *3*(2), 105–115.
Mousavi, M., Ghafory-Ashtiany, M., & Azarbakht, A. (2011). A new indicator of elastic spectral shape for the reliable selection of ground motion records. *Earthquake Engineering & Structural Dynamics*, *40*(12), 1403–1416.
Okuwaki, R., Yagi, Y., Taymaz, T., & Hicks, S. P. (2023). Multi-Scale Rupture Growth With Alternating Directions in a Complex Fault Network During the 2023 South-Eastern Türkiye and Syria Earthquake Doublet. *Geophysical Research Letters*, *50*(12), e2023GL103480.
Ozkula, G., Dowell, R. K., Baser, T., Lin, J.-L., Numanoglu, O. A., Ilhan, O., Olgun, C. G., Huang, C.-W., & Uludag, T. D. (2023). Field reconnaissance and observations from the February 6, 2023, Turkey earthquake sequence. *Natural Hazards*, 1–38.
Paolucci, R., Pacor, F., Puglia, R., Ameri, G., Cauzzi, C., & Massa, M. (2011). Record processing in ITACA, the new Italian strong-motion database. *Earthquake Data in Engineering Seismology: Predictive Models, Data Management and Networks*, 99–113.
Poulos, A., & Miranda, E. (2022a). Probabilistic characterization of the directionality of horizontal earthquake response spectra. *Earthquake Engineering & Structural Dynamics*, *51*(9), 2077–2090.
Poulos, A., & Miranda, E. (2022b). Proposal of orientation-independent measure of intensity for earthquake-resistant design. *Earthquake Spectra*, *38*(1), 235–253.
Poulos, A., & Miranda, E. (2023). *Effect of style of faulting on the orientation of maximum horizontal earthquake response spectra*.
Savage, J. C. (1965). The stopping phase on seismograms. *Bulletin of the Seismological Society of America*, *55*(1), 47–58.
Shome, N. (1999). *Probabilistic seismic demand analysis of nonlinear structures*. Stanford University.
Shome, N., Cornell, C. A., Bazzurro, P., & Carballo, J. E. (1998). Earthquakes, records, and nonlinear responses. *Earthquake Spectra*, *14*(3), 469–500.
Song, S. (2014). *A new ground motion intensity measure, Peak Filtered Acceleration (PFA), to estimate collapse vulnerability of buildings in earthquakes*. California Institute of Technology.
Taymaz, T., Eyidoğan, H., & Jackson, J. (1991). Source parameters of large earthquakes in the East Anatolian Fault Zone (Turkey). *Geophysical Journal International*, *106*(3), 537–550.
Tothong, P., & Luco, N. (2007). Probabilistic seismic demand analysis using advanced ground motion intensity measures. *Earthquake Engineering & Structural Dynamics*, *36*(13), 1837–1860.

USGS. (2023a). *M 7.5 – Elbistan earthquake, Kahramanmaras 618 earthquake sequence*. https://earthquake.usgs.gov/earthquakes/eventpage/us6000jlqa/executive

USGS. (2023b). *M 7.8 - Pazarcik earthquake, Kahramanmaras 615 earthquake sequence*. https://earthquake.usgs.gov/earthquakes/eventpage/us6000jllz/executive

Vamvatsikos, D., & Cornell, C. A. (2002). Incremental dynamic analysis. *Earthquake Engineering \& Structural Dynamics*, *31*(3), 491–514.

Yakhchalian, M., Nicknam, A., & Amiri, G. G. (2015). Optimal vector-valued intensity measure for seismic collapse assessment of structures. *Earthquake Engineering and Engineering Vibration*, *14*, 37–54.